


Probing elastic anisotropy on entropic interfaces

Ye Yuan,^{1,*} Paride Azzari,¹ and Raffaele Mezzenga^{1,2,†}

¹Department of Health Sciences and Technology, *ETH Zurich*, Zurich 8092, Switzerland

²Department of Materials, *ETH Zurich*, Zurich 8093, Switzerland

 (Received 12 October 2023; revised 8 February 2024; accepted 27 June 2024; published 29 July 2024)

Liquid-liquid phase separation is vital in the formation of many biomolecular condensates, including cellular membraneless organelles. When semiflexible macromolecules are involved, the process switches from mostly enthalpy- to dominantly entropy-driven, changing the intrinsic nature of the interfaces and bringing new physical traits. Here, we present a concept to address the complexity of entropic interfaces where laser trapping and microscopy are combined to capture the behavior of probe colloidal particles onto liquid crystalline droplet surfaces. Hertz-Frank-Oseen contact theory is extended to calculate the elasticity of the droplet based on particle trajectories. We show that this method is sensitive enough to resolve the anisotropic elasticity originating from the collective molecular orientation of constitutive semiflexible mesogens, introducing a possible tool to assess biomechanics of cellular and molecular condensates.

DOI: [10.1103/PhysRevResearch.6.033118](https://doi.org/10.1103/PhysRevResearch.6.033118)

I. INTRODUCTION

Liquid-liquid phase separation (LLPS) mostly results from the demixing of an initially homogeneous fluid undergoing a change in the enthalpy of interaction among their immiscible constituents [1]. In this process, the molecules aggregate with their own kind to lower the total enthalpic cost of interactions, at the expense of entropy which favors mixing; yet if this trade-off results in an overall decrease of the free energy of mixing, LLPS will take place [2]. Interestingly, this newborn heterogeneous system can provide a suitable environment for biochemical reactions. For example, nucleoli as the largest membraneless organelles in eukaryotic cells are assemblies of proteins and nucleic acids phase separated from the nucleoplasm to produce ribosome subunits [3]. A handful of other cellular compartments generated by LLPS are found in both the nucleus and the cytoplasm and participate in important cellular functions [4–7] including gene expression and stress response. While many of these biomacromolecular condensates share common properties such as being spherical in shape due to surface tension, easily deformable, and allowing for rapid exchange of materials with environments, some deviate from the typical liquid droplet behavior [8], suggesting other formation mechanisms and functionalities. The

role of LLPS in biology is thus receiving steadily increasing attention.

When the constituent macromolecules are more rigid, their behavior is better described by liquid crystal (LC) theories where, due to the high excluded volume of the molecules, i.e., the mesogens, the phase separation process becomes predominantly entropy-driven [9]. This is observed, for example, in suspensions of collagen, actin, microtubules, amyloids for protein-based systems, cellulose or chitin for polysaccharides, as well as filamentous viruses for hybrid biological molecules, to cite only a few examples [10]. This phenomenon, which is more appropriately referred to as liquid-liquid crystalline phase separation (LLCPS) [11,12], is responsible for the genesis of LC droplets, i.e., tactoids, where the rigid macromolecules up-concentrate spontaneously by nucleation and growth from an initially homogeneous suspension. The switch in the free energy of the system from enthalpy controlled to entropy dominated endows droplets generated via LLCPS with several totally different physical features that LLPS droplets do not have. Particularly noteworthy are the non-spherical shapes of the tactoids (spindlelike, prolatelike, and lenticular), their distinct composition (a single mesogen component in water, with significantly larger water content), anisotropic dielectric, optical and mechanical properties, and vanishingly small surface tensions, up to 10–100 times lower than in the LLPS case [13]. Perhaps one of the most stunning features of LLCPS droplets: even their surface gains anisotropic features stemming from an entropic origin [14].

While a theoretical treatment of the anisotropic behavior of entropic interfaces has been proposed and used [15], experimental approaches are lacking. The main method attempts to indirectly extract via shape analysis of the droplets the two main components of the interfacial tension postulated by the theory: the isotropic and anchoring terms [16]. However, this method is limited to treating specific configurations of the nematic fields [17,18] and entirely mirrors the success and

*Present address: International Institute for Sustainability with Knotted Chiral Meta Matter (WPI-SKCM²), Hiroshima University, 1-3-1 Kagamiyama, Higashi-Hiroshima, Hiroshima 739-8526, Japan.

†Contact author: Raffaele.Mezzenga@hest.ethz.ch

Published by the American Physical Society under the terms of the [Creative Commons Attribution 4.0 International](https://creativecommons.org/licenses/by/4.0/) license. Further distribution of this work must maintain attribution to the author(s) and the published article's title, journal citation, and DOI.

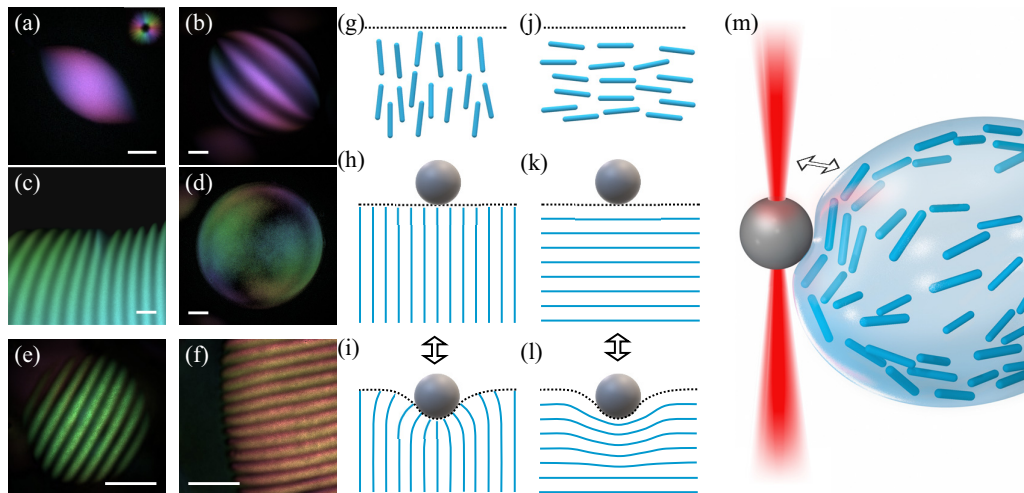


FIG. 1. Tactoids and director fields deformed by microspheres on interfaces. Micrographs of various tactoids formed spontaneously in aqueous suspensions of amyloid fibrils, including (a) bipolar, (b) and (c) uniaxial cholesteric, and (d) spherical tactoids. (e) and (f) Micrographs of cholesteric tactoids in cellulose nanocrystal aqueous suspensions. The micrographs are taken using a PolScope setup, and the color represents the director orientation; the color scheme is shown as an inset in (a). Scale bars are $20\ \mu\text{m}$. (g) and (j) Schematics showing liquid crystal (LC) molecular orientations in the vicinity of the tactoid boundaries with homeotropic and planar surface anchoring, respectively. The dotted lines indicate the tactoid-isotropic suspension interface, and the blue rods represent the LC molecules. Schematics showing the deformation of the interfaces and director fields caused by microspheres pushing into (h) and (i) homeotropic, and (k) and (l) planar interfaces. The solid blue lines represent director fields. (m) Three-dimensional (3D) schematic showing the setup of the experiments: A microsphere is brought into contact with a tactoid by a laser trap (red beam), causing deformation of the tactoid and LC molecular reorientation. The schematics are not drawn true to scale.

limits of the Rapini-Papoular formulation of the interfacial tension. An approach directly probing and measuring the complex behavior of entropic and anisotropic interfaces *in situ* is yet to be found. Here, we demonstrate that LC anisotropic elasticity at droplet entropic interfaces can be measured locally and precisely by observing the time-dependent trajectory of colloidal probe particles as they are pushed away by the deformed tactoid surface, resorting to its equilibrium shape (see schematics in Fig. 1). The dynamics of the particles is altered when they are placed, with the help of optical tweezers, on tactoid surfaces with different anchoring of the mesogens, thus capturing the elasticity anisotropy at length scales typical of the probe particle used. We use LLCPS from aqueous suspensions of cellulose nanocrystals (CNCs) and amyloid fibrils (AFs) as model filamentous colloids to demonstrate the generality and the power of this approach; we then validate it on a multitude of experimental cases of tactoids with diverse nematic field configurations, including bipolar, monoaxial, and radial cholesteric, demonstrating the broad scope of this methodology. Finally, we discuss possible implications of this treatment by extension also to nonentropic interfaces, with direct significance to systems stemming from LLPS rather than LLCPS.

II. RESULTS

A. Colloidal contact mechanics

Tactoids emerge spontaneously in aqueous solutions of filamentous mesogens and vary in size, symmetry, and director configurations, from spindle-like bipolar to spherical with helical twisting director field (Fig. 1 and Fig. S1 in the Supplemental Material [19]). To attack the analysis in a

tractable way, we first study the interaction of the probing particle with a flat interface, i.e., the boundary of a large tactoid with small surface curvature. Experimentally, such tactoids can be found in a phase-separated solution of CNCs (Fig. 2). Codispersed with the CNCs are polystyrene microspheres with a diameter of $5\ \mu\text{m}$ capped with polyethylene glycol to minimize their surface charge. The probing sphere is then captured by a laser tweezer, brought close to and pushed into the flat side of the tactoid at the speed of $<10\ \mu\text{m/s}$. During the process, the interface and the underlying director field bend to accommodate the indentation but prevent the probe sphere from penetrating through. When the indentation of the sphere is comparable with its diameter, i.e., a few microns, the pushing is stopped, and the system is allowed 10 s to equilibrate before the laser trap is removed. The sphere is observed to be pushed back by the interface, while the tactoid along with the director field within restores to its original state (Figs. 2 and 3, and Fig. S2 in the Supplemental Material [19]). This process takes 1–3 min. The time-dependent trajectories of the probing spheres are then extracted from microscopic videos for quantitative analysis.

The system can be modeled as the interaction between a sphere and a volume filling half of the space, like the Hertz contact mechanics [20,21]. The key difference is that, here, since the half space is liquid crystalline, the elasticity is anisotropic, depending on the configuration of the underlying director field and the direction of interaction. Two representative cases are when the mesogens are aligned perpendicular and parallel to the interface [compare Figs. 1(g)–1(i) and Figs. 1(j)–1(l)] where the splay and bend elasticity (characterized by K_1 and K_3 in the Frank-Oseen free energy expression) is engaged [22], respectively. In doing so, we note that the

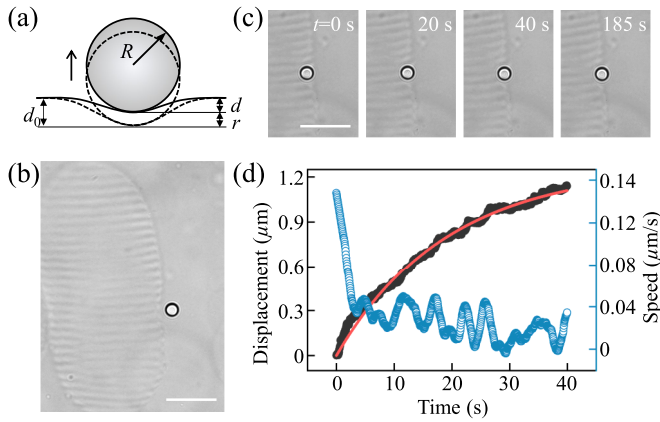


FIG. 2. Kinematics of a microsphere after indenting a tactoid with small initial surface curvature. (a) Schematic showing the definitions of parameters in the kinematic analysis; R is the radius of the probing sphere, r the displacement of the sphere, d the indentation, and d_0 the initial indentation when the sphere is released from the laser tweezer. Dashed lines indicate the starting position of the system. (b) Micrograph of a probing sphere brought close to a large tactoid with flat boundary sections, i.e., with small curvature. (c) Snapshots of the movement of the microsphere being pushed out after released from the laser trap at $t = 0$ s. Scale bars are $20 \mu\text{m}$. (d) The displacement and speed vs time of the microsphere extracted from tracking the movement of the sphere in (c). The solid red lines are the fitted curve of the displacement vs time data using the expression $r(t) = d_0(1 - e^{-\alpha t})$.

energetic cost from the twisting contribution is ignored, due to the fact that (i) the indentation induces, predominantly, bend and splay deformations, and (ii) the twist elastic constant K_2 is usually an order of magnitude smaller than K_1 and K_3 for filamentous colloids [16]. Furthermore, as a further approximation, the contribution from the saddle splay deformation is also omitted from the Frank-Oseen free energy functional because its significance in lyotropic LCs of filamentous meso-

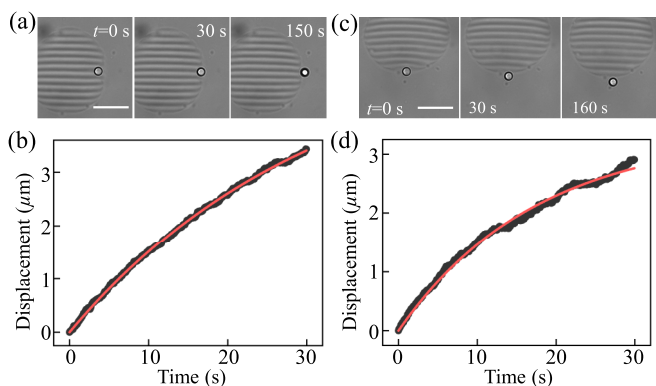


FIG. 3. Measuring elastic anisotropy on cellulose nanocrystal (CNC) tactoids by analyzing microsphere kinematics interacting in orthogonal directions. (a) and (c) Snapshots of the movement of microspheres after released from the laser trap at $t = 0$ s. Scale bars are $20 \mu\text{m}$. (b) and (d) Experimental data and the fitted curves (solid red line) of displacement vs time extracted from the corresponding videos.

gens such as CNC and AF is minor, and shape, morphology, and viscoelastic properties in tactoids made thereof have been successfully interpreted without explicitly accounting for it [16,18,23,24]. The other most significant factors considered include the surface tension and the viscosity of the fluid that surrounds the probe sphere.

Under the low Reynold's number approximation [25], the elastic forces from both the LC and the interface are balanced by the viscous force of the surrounding liquid, leading to the equation $-6\pi\eta R\dot{d} = 2d(2\gamma + K_i/R)$, $i = 1, 3$, where η is the viscosity of the surrounding isotropic phase, γ is the surface tension, and R is the radius of the probing sphere. Solving this equation yields the time-dependent displacement of the probing sphere $r(t) = d_0(1 - e^{-\alpha t})$, where d_0 is the initial indentation of the interface at $t = 0$ s when the sphere is released from the laser trap. The characteristic time scale factor α is expressed as $\alpha = (2\gamma + K_i/R)/3\eta R$ (the full derivation of this extended Hertz approach is described in detail in Appendix B). From this expression, the elastic constants can be calculated using known values of η (measured experimentally, see Fig. S3 in the Supplemental Material [19] and discussions in Appendix B) and γ [16] (values and derivation detailed in Appendix B) and by fitting the experimental curves of motion to obtain α . In this case, the calculation yields a splay elastic constant $K_1 = 4.9$ pN, consistent with previous reported values [16]. This free energy analysis including the LC director distortions is further warranted given the extrapolation length of the CNC solution [16,26] estimated from $K/\gamma \sim 10 \mu\text{m}$, comparable with the size of the probe sphere. We additionally note that the treatment above assumes, without loss of generality, an isotropic surface tension γ , over a more general anisotropic surface tension including also the anchoring contribution $\sim \gamma\omega$, with ω the anchoring strength. This effect is, however, minor and deemed negligible for the estimation of K_3 since, in bend mode, the anchoring part of the surface energy is zero due to the parallel anchoring of the mesogens and small for the estimation of K_1 where the mesogens are in homeotropic orientation. This residual small uncertainty in K_1 can be further removed by replacing γ by $\gamma(1 + \omega)$ once the anchoring strength is known [16] and by considering the tactoidal particle spheroidal [24]. Thus, on different interfaces with other underlying director field and formed by different mesogens, material-dependent and local elastic constants can also be measured using this method, as discussed below.

B. Probing elastic anisotropy

The collective molecular orientation of the constitutive mesogens in LCs is the symmetry-breaking origin from which the anisotropic properties of LCs result, including optical birefringence, dielectric and magnetic susceptibility anisotropy, as well as direction-dependent mechanical responses characterized by the elastic constants [22]. Microscopically, the mechanical anisotropy also manifests through anisotropic Brownian motion of colloidal particles suspended in LCs and long-range elasticity-mediated colloidal interactions [27]. Therefore, it is expected that interfaces enclosing different director configurations produce different dynamics of the probing spheres contacting the interfaces.

Ideally, it is best to observe the kinematics of the probing spheres on the same flat interfaces with different underlying director fields. However, the tactoidal nature of the LLCPS only allows the generation of droplets with rounded surfaces, and carrying out the measurements on different tactoids risks taking uncontrollable environmental variations, such as the intrinsic differences in mechanical and viscous properties of both the tactoid and surrounding isotropic phase resulting from the variation of local mesogen concentration. This dilemma is resolved by using a spherical tactoid with uniaxial cholesteric director field, whose size (diameter $\sim 50 \mu\text{m}$) is much larger than the diameter of the probing sphere ($\sim 5 \mu\text{m}$; Fig. 3). When the probing sphere is pushed into the tactoid parallel and perpendicular to the cholesteric layers, splay and bend distortions are primarily and respectively induced and engaged to propel the microsphere out. The small curvature of the interface compared with that of the probing spheres allows for the approximation of flat surfaces, as in the Hertz contact mechanics. Additionally, the spherical shape ensures that the curvature of the contact points on the interface are the same in both cases, minimizing the effect of the surface morphology on the ensuing particle dynamics.

This method indeed allows resolving the elastic anisotropy, yielding 3.7 and 10 pN as the values of the splay and bend elastic constants. The difference is more than twofold, which also agrees with previous theoretical and experimental results that the bend constant is larger than the splay constant [16,28]. Repetitive experimental measurements using another spherical tactoid are made and found to give similar values of both constants 4.3 and 7.1 pN, respectively (Fig. S4 in the Supplemental Material [19]). The differences among the values of the same constant measured over different tactoid droplets are expected and can be explained by the different geometry of the interfaces (radius of curvature of the tactoids) and the different compositions across tactoids at different stages of the nucleation and growth phase separation process [11]. Nonetheless, even when these physical differences among different tactoids are considered, the precision of the proposed method is remarkable when benchmarked against the current state of the art (see Table I). Thus, the consistency of the elastic anisotropy measured and the agreement with previous reports strongly suggest that this is a consistent and reproducible method for probing mechanical properties in LLPS/LLCPS systems.

C. Material-dependent elasticity

Changes in properties among different classes of materials can also be detected. Differently from the polysaccharide nature of the CNCs, AFs are stable proteinaceous nanofilaments originally found in pathogenic plaques related to neurodegenerative diseases [29]. Synthetic AFs of 4 nm in diameter and up to a few microns in length are used here to access tactoid interfaces of different kinds, notably, bipolar and radial cholesteric tactoids that do not exist in CNC-based systems [24]. Additionally, the surface tension at the interfaces in the AF solutions differ from that of the CNC solutions given the differences in the molecular geometry and charge [16]; the AF solutions are also less viscous when sheared at the same rate (Fig. S3 in the Supplemental Material [19]). With these

TABLE I. Measured values of elastic constants. Listed are the values of the fitting parameters α and d_0 from the equation of motion of the probing spheres after released from the laser trap as well as the elastic constants calculated from α . Elastic constant values without following paratheses are the bend constants K_3 . The values in italics are measurements from the same spherical tactoid with uniaxial cholesteric director distribution, and the bold ones are repetitive measurements with another such spherical tactoid. The graph on the right shows the measured values (in darker shaded bars) in comparison to previous reports [16] (in lighter shaded bars). The blue shaded bars represent the values of the splay constant (K_1) and the orange ones the bend constant (K_3).

α	d_0 (μm)	K_i (pN)
<i>AF</i>		
0.085	4.9	2.5
0.071	4.2	1.9
0.060	6.8	1.5
0.073	3.1	2.0
0.074	3.6	2.0 (K_1)
0.064	2.9	1.6 (K_1)
0.073	3.6	2.0 (K_1)
0.035	3.2	0.46
<i>CNC</i>		
0.031	5.7	3.7 (K_1)
0.076	2.8	10
0.040	3.2	5.0
0.039	3.9	4.9 (K_1)
0.035	3.4	4.3 (K_1)
0.055	2.6	7.1

differences considered, the splay and bend elastic constants of amyloid-based LC are found to be around 2 pN, smaller than that of the CNC-based system (Fig. 4 and Table I, and Fig. S5 and Table S1 in the Supplemental Material [19]). The convergence of the measurement also indicates that the flat-surface approximation in the contact mechanics analysis is valid. Additionally, the difference between the elastic constants K_1 and K_3 is not significant (Table I), also consistent with previous studies [16] on AF LCs. Interestingly, the value measured against a small tactoid with the dimension comparable with that of the probing sphere is only 0.61 pN, much smaller than the rest [Fig. 4(g)]. This is an expected breakdown of the analysis because of its deviation from the model: the small tactoid cannot be treated as an elastic material filling half of the space.

III. DISCUSSION

Obtaining the magnitude of elastic constants is a central topic in the research of LCs, for they determine the response to external electromagnetic fields, elasticity-mediated colloidal interactions, formation of topological defects, and many other characteristic and unique behaviors of LC materials [22,25,26]. However, the experimental measurement of elastic constants remains a challenge because of the difficulty in exciting only one type of director distortion, that is, involving only one elastic constant [30]. The Fréedericksz transition is often used in such measurements, but it is limited to

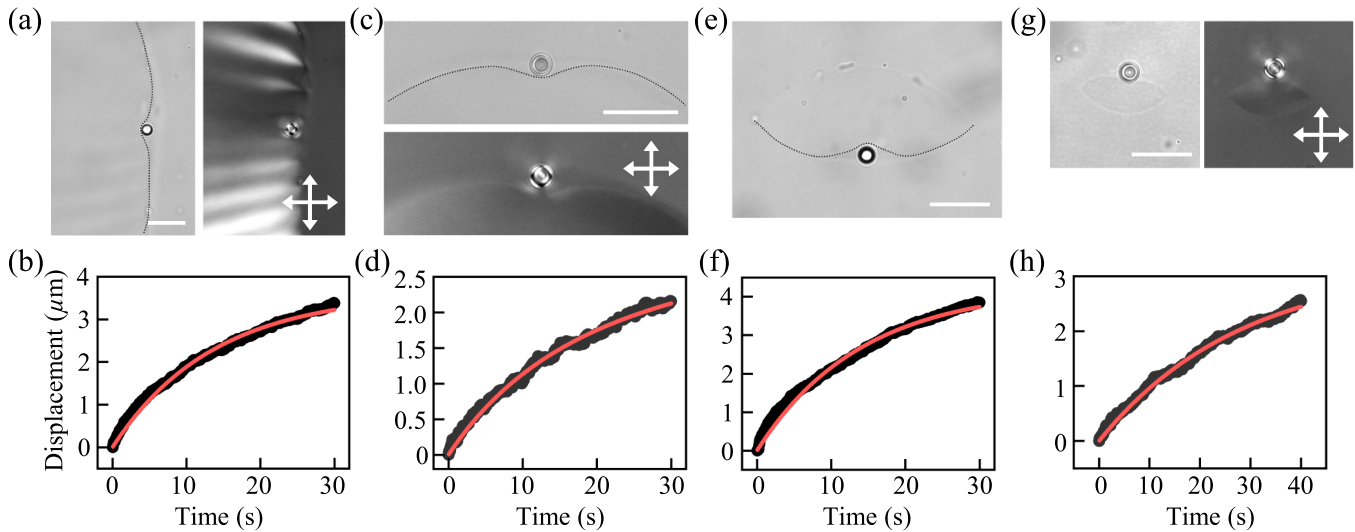


FIG. 4. Elasticity measurement using amyloid fibril (AF) tactoids with various director configurations and shapes. Micrographs of microspheres on the interfaces of (a) cholesteric, (d) spherical, (e) large bipolar, and (g) small bipolar tactoids in AF suspensions. Dotted lines are for eye guidance, indicating the interfaces. Insets with a dark background were taken under crossed polarizers (marked with white double arrows). Scale bars are $20\ \mu\text{m}$. (b), (d), (f), and (h) The corresponding experimental and fitted data of displacement vs time after the spheres were released from the laser tweezer.

LCs with strong electromagnetic responses, most commonly in thermotropic and some lyotropic LCs including aqueous solution of rodlike virus and synthetic polymers [31–36]. However, this method is not applicable to many other lyotropic LCs consisting of biological semiflexible polymers such as CNC and AF with low anisotropy in electric or magnetic susceptibility, the measurement of which must resort to other methods [37–39]. These limitations can be overcome with the method presented here, where the measurement is independent of external fields and can be extended to measuring the elastic constants of any types of LCs, provided that an interface is established for the probing colloidal particle to interact with. The interface is not limited to the surface of LC droplets but can be any boundaries separating LCs and the other immiscible liquids with suitable viscosity and interfacial tension [40].

Moreover, this method can be extended to other phase-separated systems to test their mesoscale mechanical properties. One notable example is biomolecular condensates that form cellular membraneless organelles. Like the entropy-driven LC tactoids, these condensates in the cytoplasm or nucleoplasm emerge when the concentration of constituting molecules reaches a certain critical value, and they may take the form of a liquid, hydrogel, or even solid, meanwhile changeable upon external stimuli. The interaction between condensates and a probing sphere or a surface can provide information about the condensates, the interface, as well as the surrounding cellular plasma. As in the examples shown above, this can be achieved by extending the Hertz contact model to include both the viscous drag and the surface tension and treating the condensate as an isotropic material. The equation describing this general case is $-6\pi\eta R\dot{d} = \frac{4}{3}E^*R^{1/2}d^{3/2} + 4\pi\gamma d$, where $E^* = E/(1 - \nu^2)$ is the effective elastic modulus calculated from the material elasticity E and its Poisson ratio ν , assuming the probing sphere is hard

and incompressible. The equation can be solved analytically in the limiting cases where either the elasticity or the surface tension is negligible as well as where contributions from both sources are comparable (see the derivation in Appendix B). The competition between the two determines the dynamics of the probing sphere after the indentation—for the surface tension dominated case, the equation of motion is exponential, and for the elasticity dominated case, it is a reciprocal of a square function (Fig. S6 in the Supplemental Material [19]). Like demonstrated above, the kinematics parameters derived from the motion of the probes can then be used to calculate the elastic modulus of the condensates, surface tension, or the viscosity of the surrounding media. Along with the biochemical study of the biomolecular condensates, investigating their mechanical response upon external stimuli may contribute to a comprehensive understanding of the function of membraneless organelles.

IV. CONCLUSIONS

Entropic interfaces in phase-separated systems provide a unique and unconventional window for looking into the subtle differences in elasticity emerging from the collective molecular orientation of the constituting semiflexible polymers because the surface tension and the LC elasticity are comparable in strength. It is shown here that such weak differences can be resolved by observing the kinematics of a probing particle during its interaction with the interface, and the measured values are consistent with previous experimental and theoretical reports yet offer significant more precision. Therefore, analyzing the dynamics of colloidal probes can serve as a complementary tool to existing direct measurement methods, such as using optical trapping or atomic force microscopy [41–44], to investigate mesoscale mechanical properties of soft materials. Just like the diverse configurations in

contact mechanics, the size and shape of the probing particles as well as the morphology of the interfaces can affect the dynamic processes, which calls for future theoretical and experimental efforts and provides the opportunity to resolve subtle effects. The application of this method may range from understanding the physical underpinnings of LLPS/LLCPS to investigating the biomechanics of cellular structures and tissues [45] and to developing therapeutic and diagnostic approaches for neurodegenerative diseases [46].

All relevant data are available in the main text or the Supplemental Material [19].

ACKNOWLEDGMENTS

We thank H. Spanke, M. Feofilova, and G. Wolfsberg in the group of E. Dufresne for providing access to the laser trapping setup. We thank Q. Sun, P. Fisher, M. Almukambetova, and J. Zhou for technical support and inspiring discussions. This paper is supported by the Sinergia Scheme Grant No. CRSII5_189917 (RM, PF) from the Swiss National Science Foundation.

APPENDIX A: MATERIALS AND METHODS

1. Sample preparation

Cellulose-based system. Sulfated CNC powder was purchased from CelluForce (Montreal, Canada) and was dispersed in Milli-Q water at 4 wt. %. The dispersion was then stirred overnight and sonicated (Hielscher UP200S, Teltow, Germany) at the power of 160 W with the energy input of 5 kJ/g. Polystyrene microspheres (PS spheres, $\phi \sim 5 \mu\text{m}$) functionalized with polyethylene glycol (PEG, Mw = 5000 Da) were purchased from Suzhou Infinity Nanotechnology (Suzhou, China) and diluted with Milli-Q water to 0.05 wt. % from the original 2.5 wt. %. Here, 5 μL of the PS sphere suspension was mixed with 35 μL of CNC dispersion and infiltrated into a 50-mm-long glass capillary tube with a cross-section of $0.2 \times 4 \text{ mm}^2$ (CM Scientific, UK). One end of the filled capillary was sealed with ultraviolet-curable glue, and the other end was left open overnight before being sealed to allow excess water to evaporate.

Amyloid-based system. AFs were synthesized using previously reported protocols [16]. Briefly, 300 mL of 2 wt. % aqueous solution of β -lactoglobulin at pH = 2 was incubated at 90 °C for 5 h, followed by quenching in an ice bath to stop the reaction and mechanic shearing to shorten the fibrils. The solution was then dialyzed (Spectra/Por dialysis membrane 1, 100 kDa) in 10 L of Milli-Q water at pH = 2 for 5 d and up-concentrated (Spectra/Por dialysis membrane 1, 6–8 kDa) to 2 wt. % again against 1 L of 6 wt. % PEG (Sigma-Aldrich, Mw = 35 kDa). The length distribution of both the AFs and CNCs can be found in previous reports [16]. The PS spheres were redispersed in pH = 2 Milli-Q water by washing in a centrifuge at the speed of 5000 rpm for 10 min. The AF and PS sphere solutions were then mixed and filled in a capillary tube using the same method described above. The viscosity of pure CNC and AF solutions was measured in a CC17 Couette installed on an Anton Paar rheometer (Physica MCR

501). Prior to the measurements, the solutions were agitated to render them isotropic.

2. Optical trapping and microscopy

The optical trapping system was constructed by integrating a 785 nm continuous laser (LUXX 785–200, Omicron Laserage Laserprodukte GmbH) into an inverted optical microscope (ECLIPSE Ti2, Nikon). The trap operated at the maximum laser power of 200 mW to capture the PS spheres and stayed stationary while the samples were moved by the positioning stage of the microscope. After the probing spheres were pushed into the tactoids at the desired depth of indentation on the interfaces, the laser was turned off so that the spheres interacted freely with the interfaces. Polarizing images and videos capturing the trajectories of the probing spheres and the changing appearance of the tactoids were recorded with a camera (ORCA-Flash 4.0, C13440, Hamamatsu) attached to the microscope. The micrographs showing the director field distribution of the samples were taken with a LC-PolScope setup (meadowlark optics) mounted on an upright microscope (AxioImager.Z2, Zeiss).

3. Data analysis

The coordinates of the probing spheres after released from the laser tweezer were extracted from the microscope videos on a frame-by-frame basis using an ImageJ [47] plugin wrMT-trck [48]. The corresponding time to the coordinates of the spheres was calculated based on the frame number and frame rate of the video (usually 20 fps). The displacement vs time of the microspheres was then plotted in Origin and fitted to an exponential expression (described below). The initial indentation d_0 and a fitting parameter α were obtained from the fitting and used to calculate the elastic constants. The speed of the sphere was calculated by taking the time derivative of the displacement and was found to be in the range of 0.1–1 $\mu\text{m/s}$.

APPENDIX B: ANALYSIS AND DERIVATIONS

1. Kinetic analysis of microspheres on entropic interfaces

After the probing sphere is released from the laser tweezer, it is pushed out of the tactoid by the restoring force from both the surface tension and the elastic distortion of the director as indicated by the Young-Laplace pressure with an additional elastic term [21]:

$$\Delta p = \frac{2}{R}\gamma + f_b, \quad (\text{B1})$$

where γ is the surface tension and f_b is the Frank-Oseen free energy density. The energy density describing the energy cost of LC director distortions of splay, twist, and bend is written as

$$f_b = K_1(\nabla \cdot n)^2 + K_2(n \cdot \nabla \times n)^2 + K_3(n \times \nabla \times n)^2,$$

where K_1 , K_2 , and K_3 are the elastic constants of splay, twist, and bend distortions, respectively. If only splay or bend distortion is involved [see Figs. 1(i) and 1(D)] and there is full contact between the sphere and interface during the indentation, the

energy density can be written as

$$f_b = \frac{K_i}{R^2}, \quad i = 1, 3,$$

where R is the radius of the sphere. The force on the sphere from the indented interface is found by multiplying Eq. (B1) with the contact area $A = 2\pi R d$:

$$F = A \Delta p = 2\pi d \left(2\gamma + \frac{K_i}{R} \right),$$

where d is the depth of indentation of the sphere into the interface. Under the low Reynold's number approximation, the inertia of the microsphere is omitted, and the Laplace force must be balanced by the viscous drag $F_d \propto v$, where v is the speed of the sphere. The Stokes law states that the drag force of the sphere in a fluid can be written as $F_d = 6\pi\eta R v$, where η is the viscosity of the fluid. Here, the speed of the sphere is $v = -\dot{d}$ (minus sign added to obtain the absolute value). Equating the two forces $F = F_d$ gives the equation of motion:

$$-6\pi\eta R \dot{d} = 2\pi d \left(2\gamma + \frac{K_i}{R} \right), \quad (\text{B2})$$

whose solution is $d(t) = d_0 e^{-\alpha t}$, with the parameter expressed as

$$\alpha = \frac{1}{3\eta R} \left(2\gamma + \frac{K_i}{R} \right),$$

given the initial condition $d(0) = d_0$. The displacement of the sphere $r(t)$ is related to the indentation by $r(t) = d_0 - d(t)$ [see Fig. 2(a) for the schematic]. Therefore, the displacement of the sphere can be written as

$$r(t) = d_0(1 - e^{-\alpha t}).$$

This expression was used to fit the experimental data obtained by tracking the motion of the spheres with d_0 and α as the fitting parameters.

The elastic constant can be calculated by rewriting the expression of α into:

$$K_i = R(3\eta R \alpha - 2\gamma),$$

and plugging in the values of η and γ . Because the viscosity η is shear dependent, it is necessary to estimate the shear rate of the surrounding liquid caused by the moving microsphere to obtain the proper viscosity. Assuming that the probing spheres are in the middle of the capillary with a thickness of $h = 0.2$ mm, the shear rate is then $\dot{d}/(h/2) \sim 0.01$ s⁻¹, with $\dot{d} \sim 1$ μm/s (see schematic in Fig. S3(a) in the Supplemental Material [19]). Therefore, from the rheometer measurement (Fig. S3(b) in the Supplemental Material [19]), the viscosities of the fluids used in the experiments are found to be 7.6 and 2.2 Pa s for CNC and AF solutions, respectively. The values of the surface tension are estimated using [14]

$$\gamma = b \frac{k_B T}{LD},$$

where k_B is the Boltzmann constant, T the room temperature, and L (D) the length (effective diameter) of the rodlike mesogens. The numerical prefactor b is chosen to be 0.18, and plugging in the same value for other parameters as in Ref. [16] of the main text (the same materials are used), the

surface tension for the CNC and AF systems are computed to be 0.14×10^{-6} and 0.20×10^{-6} N/m, respectively. The elastic constants are then calculated combining the values of α , η , and γ , and are listed in Table I and Table S1 in the Supplemental Material [19].

2. Extended Hertz contact mechanics

Hertz contact mechanics states that the force on the probing sphere indenting an elastic material filling half of the space is [20]

$$F_H = \frac{4}{3} E^* R^{1/2} d^{3/2},$$

where the effective elastic modulus $E^* = \frac{E}{1-\nu^2}$ is related to the material elasticity E and its Poisson ratio ν , assuming a hard, noncompressible probing sphere. Additional restoring force is supplied by the surface tension using Young-Laplace pressure and the contact area A :

$$F_S = \frac{2}{R} \gamma A = 4\pi \gamma d.$$

Balancing the forces $F_d = F_H + F_S$ results in a nonlinear differential equation:

$$-6\pi\eta R \dot{d} = \frac{4}{3} E^* R^{1/2} d^{3/2} + 4\pi \gamma d. \quad (\text{B3})$$

This equation is to be seen as the limiting case of Eq. (B2) developed for anisotropic materials, this time extrapolated to the case of isotropic materials, although Eq. (B2) uses Frank-Oseen formalism and Eq. (B3) Hertz language (hence the different scaling of d for the two expressions).

Equation (B3) can be simplified for special cases. For example, if the material is purely viscous, i.e., $E = 0$ as in a liquid, the equation reduces to

$$\dot{d} = -\frac{2}{3} \frac{\gamma}{\eta R} d.$$

This is equivalent to the previous case when we set $K_i = 0$, and the solution would be exponential $d(t) = d_0 e^{-\alpha' t}$, where

$$\alpha' = \frac{2\gamma}{3\eta R}.$$

In another case where the surface tension is negligible like that in the assumption of the original Hertz model, Eq. (B3) becomes

$$\dot{d} = -\frac{2}{9\pi} \frac{E^*}{\eta \sqrt{R}} d^{3/2},$$

which has as an analytical solution:

$$d(t) = \frac{d_0}{(1 + \alpha'' t)^2},$$

with the parameter α'' expressed as

$$\alpha'' = \frac{1}{9\pi} \frac{E^* \sqrt{d_0}}{\eta \sqrt{R}},$$

or the displacement of the probing sphere can be written as

$$r(t) = d_0 \left[1 - \frac{1}{(1 + \alpha'' t)^2} \right].$$

Both α' and α'' have dependencies on material properties such as the surface tension and elasticity and can be used to calculate the values of these properties by fitting the experimental data.

Equation (B3) can also be solved analytically without the above approximations. To analyze the effect of the elasticity or the surface tension on the system dynamics, we can parameterize Eq. (B3) by defining $t = 6\pi\eta R\tau$ and $d = d_0x(\tau)$. The equation then turns into

$$\dot{x} = -C_E x^{3/2} - C_S x, \quad (\text{B4})$$

where $C_E = 4E^*R^{1/2}d_0^{1/2}/3$ and $C_S = 4\pi\gamma$, corresponding to the contribution from the elasticity and the surface tension. Under the same parametrization, the dimensionless displacement becomes

$$\frac{r(\tau)}{d_0} = 1 - x(\tau).$$

Solving Eq. (B4) gives the following solution expressed in C_E , C_S , and τ :

$$\frac{r(\tau)}{d_0} = 1 - \frac{1}{\left[\frac{C_E}{C_S} - \left(\frac{C_E}{C_S} + 1\right)\exp\left(\frac{C_S}{2}\tau\right)\right]^2}. \quad (\text{B5})$$

Substituting back the parameters, the solution for this general case reads

$$r(t) = d_0 - \frac{d_0}{\left[\frac{d_0^{1/2}R^{1/2}E^*}{3\pi\gamma} - \left(\frac{d_0^{1/2}R^{1/2}E^*}{3\pi\gamma} + 1\right)\exp\left(\frac{\gamma}{3R\eta}t\right)\right]^2}.$$

By taking the limits of $C_E \ll C_S$ and $C_E \gg C_S$ and using the Taylor expansion, this solution is shown to reduce to the solutions in the two extreme cases discussed previously.

Plotting this solution under varying ratio between C_E and C_S , we can see the transition of the solution from an exponential to a reciprocal of a square function (Fig. S6 in the Supplemental Material [19]).

-
- [1] L. D. Landau and E. M. Lifshitz, *Statistical Physics* (Pergamon Press, Oxford, 1969).
- [2] P. J. Flory, *Principles of Polymer Chemistry* (Cornell University Press, Ithaca, 1953).
- [3] C. P. Brangwynne, T. J. Mitchison, and A. A. Hyman, Active liquid-like behavior of nucleoli determines their size and shape in *Xenopus laevis* oocytes, *Proc. Natl. Acad. Sci. USA* **108**, 4334 (2011).
- [4] C. P. Brangwynne, C. Eckmann, D. S. Courson, A. Rybarska, C. Hoegge, J. Gharakhani, F. Jülicher, and A. A. Hyman, Germline P granules are liquid droplets that localize by controlled dissolution/condensation, *Science* **324**, 1729 (2009).
- [5] T. Hirose, K. Ninomiya, S. Nakagawa, and T. Yamazaki, A guide to membraneless organelles and their various roles in gene regulation, *Nat. Rev. Mol. Cell Biol.* **24**, 288 (2023).
- [6] M. Hondele, S. Heinrich, P. de los Rios, and K. Weis, Membraneless organelles: Phasing out of equilibrium, *Emerg. Top. Life Sci.* **4**, 343 (2020).
- [7] A. A. Hyman, C. A. Weber, and F. Jülicher, Liquid-liquid phase separation in biology, *Annu. Rev. Cell Dev. Biol.* **30**, 39 (2014).
- [8] S. Boeynaems, S. Alberti, N. L. Fawzi, T. Mittag, M. Polymenidou, F. Rousseau, J. Schymkowitz, J. Shorter, B. Wolozin, L. Van Den Bosch *et al.*, Protein phase separation: A new phase in cell biology, *Trends Cell Biol.* **28**, 420 (2018).
- [9] L. Onsager, The effects of shape on the interaction of colloidal particles, *Ann. N.Y. Acad. Sci.* **51**, 627 (1949).
- [10] B. L. Tardy, B. D. Mattos, C. G. Otoni, M. Beaumont, J. Majoinen, T. Kämäräinen, and O. J. Rojas, Deconstruction and reassembly of renewable polymers and biocolloids into next generation structured materials, *Chem. Rev.* **121**, 14088 (2021).
- [11] P. Azzari, M. Bagnani, and R. Mezzenga, Liquid-liquid crystalline phase separation in biological filamentous colloids: Nucleation, growth and order-order transitions of cholesteric tactoids, *Soft Matter* **17**, 6627 (2021).
- [12] P. Azzari and R. Mezzenga, LLPS vs LLCPS: Analogies and differences, *Soft Matter* **19**, 1873 (2023).
- [13] D. L. Koch and O. G. Harlen, Interfacial tension at the boundary between nematic and isotropic phases of a hard rod solution, *Macromolecules* **32**, 219 (1999).
- [14] P. van der Shoot, Remarks on the interfacial tension in colloidal systems, *Phys. Chem. B* **103**, 8804 (1999).
- [15] A. Rapini and M. Papoular, Distorsion d'une lamelle nématique sous champ magnétique conditions d'ancrage aux parois, *J. Phys. Colloques* **30**, C4-54 (1969).
- [16] M. Bagnani, P. Azzari, C. de Michele, M. Arcari, and R. Mezzenga, Elastic constants of biological filamentous colloids: Estimation and implications on nematic and cholesteric tactoid morphologies, *Soft Matter* **17**, 2158 (2021).
- [17] G. Wulff, Zur Frage der Geschwindigkeit des Wachstums und der Auflösung der Krystallflagen, *Z. Krystallog. Min.* **34**, 449 (1901).
- [18] P. Prinsen and P. van der Schoot, Shape and director-field transformation of tactoids, *Phys. Rev. E* **68**, 021701 (2003).
- [19] See Supplemental Material at <http://link.aps.org/supplemental/10.1103/PhysRevResearch.6.033118> for supplemental figures and data.
- [20] A. C. Fischer-Cripps, *Introduction to Contact Mechanics* (Springer, New York, 2000).
- [21] A. D. Rey, Young-Laplace equation for liquid crystal interfaces, *J. Chem. Phys.* **113**, 10820 (2000).
- [22] G. de Gennes and J. Prost, *The Physics of Liquid Crystals* (Oxford University Press, Oxford, 1993).
- [23] M. Bagnani, P. Azzari, S. Assenza, and R. Mezzenga, Six-fold director field configuration in amyloid nematic and cholesteric phases, *Sci. Rep.* **9**, 12654 (2019).
- [24] G. Nyström, M. Arcari, and R. Mezzenga, Confinement-induced liquid crystalline transitions in amyloid fibril cholesteric tactoids, *Nat. Nanotech.* **13**, 330 (2018).
- [25] H. Stark, Physics of colloidal dispersions in nematic liquid crystals, *Phys. Rep.* **351**, 387 (2001).
- [26] S. Wolfsheimer, K. Shundyak, C. Tanase, R. van Roij, and T. Schilling, Isotropic-nematic interface in suspensions of hard rods: Mean-field properties and capillary waves, *Phys. Rev. E* **73**, 061703 (2006).

- [27] I. I. Smalyukh, Liquid crystal colloids, *Annu. Rev. Condens. Matter Phys.* **9**, 207 (2018).
- [28] T. Odijk, Elastic constants of nematic solutions of rod-like and semi-flexible polymers, *Liq. Cryst.* **1**, 553 (1986).
- [29] D. Eisenberg and M. Jucker, The amyloid state of proteins in human diseases, *Cell* **148**, 1188 (2012).
- [30] A. A. Joshi, J. K. Whitmer, O. Guzmán, N. L. Abbott, and J. J. De Pablo, Measuring liquid crystal elastic constants with free energy perturbations, *Soft Matter* **10**, 882 (2014).
- [31] A. J. Hurd, S. Fraden, F. Lonberg, and R. B. Meyer, Field-induced transient periodic structures in nematic liquid crystals: The splay Frederiks transition, *J. Physique* **46**, 905 (1985).
- [32] V. G. Taratuta, F. Lonberg, and R. B. Meyer, Anisotropic mechanical properties of a polymer nematic liquid crystal, *Phys. Rev. A* **37**, 1831 (1988).
- [33] R. Meyer, F. Lonberg, V. Taratuta, S. Fraden, S. Lee, and A. J. Hurd, Measurements of the anisotropic viscous and elastic properties of lyotropic polymer nematics, *Faraday Discuss. Chem. Soc.* **79**, 125 (1985).
- [34] T. Sato and A. Teramoto, On the Frank elastic constants of lyotropic polymer liquid crystals, *Macromolecules* **29**, 4107 (1996).
- [35] Z. Dogic and S. Fraden, Cholesteric phase in virus suspensions, *Langmuir* **16**, 7820 (2000).
- [36] S. Zhou, Y. A. Nastishin, M. M. Omelchenko, L. Tortora, V. G. Nazarenko, O. P. Boiko, T. Ostapenko, T. Hu, C. C. Almasan, S. N. Sprunt *et al.*, Elasticity of lyotropic chromonic liquid crystals probed by director reorientation in a magnetic field, *Phys. Rev. Lett.* **109**, 037801 (2012).
- [37] L. Lucchetti, T. P. Fraccia, G. Nava, T. Turiv, F. Ciciulla, L. Bethge, S. Klussmann, O. D. Lavrentovich, and T. Bellini, Elasticity and viscosity of DNA liquid crystals, *ACS Macro Lett.* **9**, 1034 (2020).
- [38] F. Giavazzi, S. Crotti, A. Speciale, F. Serra, G. Zanchetta, V. Trappe, M. Buscaglia, T. Bellini, and R. Cerbino, Viscoelasticity of nematic liquid crystals at a glance, *Soft Matter* **10**, 3938 (2014).
- [39] O. J. Dammone, I. Zacharoudiou, R. P. A. Dullens, J. M. Yeomans, M. P. Lettinga, and D. G. A. L. Aarts, Confinement induced splay-to-bend transition of colloidal rods, *Phys. Rev. Lett.* **109**, 108303 (2012).
- [40] K. L. Weirich, S. Banerjee, K. Dasbiswas, T. A. Witten, S. Vaikuntanathan, and M. L. Gardel, Liquid behavior of cross-linked actin bundles, *Proc. Natl. Acad. Sci. USA* **114**, 2131 (2017).
- [41] F. Català-Castro, E. Schäffer, and M. Krieg, Exploring cell and tissue mechanics with optical tweezers, *J. Cell Sci.* **135**, jcs259355 (2022).
- [42] M. Krieg, G. Fläschner, D. Alsteens, B. M. Gaub, W. H. Roos, G. J. L. Wuite, H. E. Gaub, C. Gerber, Y. F. Dufrêne, and D. J. Müller, Atomic force microscopy-based mechanobiology, *Nat. Rev. Phys.* **1**, 41 (2019).
- [43] A. Morshed, B. I. Karawdeniya, Y. M. Nuwan, D. Y. Bandara, M. J. Kim, and P. Dutta, Mechanical characterization of vesicles and cells: A review, *Electrophoresis* **41**, 449 (2020).
- [44] C. Arbore, L. Perego, M. Sergides, and M. Capitanio, Probing force in living cells with optical tweezers: From single-molecule mechanics to cell mechanotransduction, *Biophys. Rev.* **11**, 765 (2019).
- [45] J. Böhning, M. Graham, S. C. Letham, L. K. Davis, U. Schulze, P. J. Stansfeld, R. A. Corey, P. Pearce, A. K. Tarafder, and T. A. M. Bharat, Biophysical basis of filamentous phage tactoid-mediated antibiotic tolerance in *P. aeruginosa*, *Nat. Commun.* **14**, 8429 (2023).
- [46] D. M. Mitrea, M. Mittasch, B. F. Gomes, I. A. Klein, and M. A. Murcko, Modulating biomolecular condensates: A novel approach to drug discovery, *Nat. Rev. Drug Discov.* **21**, 841 (2022).
- [47] ImageJ freeware from <https://www.nih.gov/>.
- [48] Plugin wrMTtrck available at <http://phage.dk/>.